

# Analytic calculation of touch and leakage currents of non-isolated EV chargers using a fast common mode calculation method and non-ideal passive component models

Christian Stutz, Sebastian Nielebock, Martin März

SIEMENS AG / FRIEDRICH-ALEXANDER-UNIVERSITY ERLANGEN-NUREMBERG

Erlangen, Germany

Tel.: +49 (1520) 3297094

E-Mail: christian.stutz@siemens.com; sebastian.nielebock@siemens.com;

martin.maerz@fau.de

URL: <https://siemens.com>; <https://www.lee.tf.fau.de/>

## Keywords

«Battery charger», «Automotive component», «Charging infrastructure for EV's», «Failure modes», «Grid-connected inverter», «Non-isolated EV chargers», «Power converters for EV», «Simulation».

## Abstract

Non-isolated charging systems suffer from tremendous touch currents due to the significant extension of the common mode coupling path by the electric vehicle. Since safety limits are very tough, the selection of converter topology, modulation scheme and filters with respect to touch current behavior is a very ambitious process. With the aim to ease integral system design, research is done for common mode analysis methods, eliminating the demand for long duration time domain simulations. A time saving method to analyze the touch current behavior in common mode domain is applied on a single stage charging system setup by a 3-level converter, filter system and a major coupling path.

Furthermore, this paper improves that time-saving failure current prediction method by including the influence of non-ideal passive component models on the calculation result. All calculation results are compared to laboratory measurements. Border conditions from corresponding standards are used to define the required frequency range. Besides the touch current, which typically occurs during the failure condition of a broken protective earth conductor, the leakage current flowing in the protective earth conductor during normal operation is analyzed. Finally, this paper points out the influence of an internal common mode bypass via the filter system on the touch and leakage current.

## 1 Introduction

### 1.1 Common mode coupling path at non-isolated charging systems

Figure 1 shows a typical two-stage electric vehicle (EV) charging system comprising an AC-DC-Converter, its filter (1. Stage), a DC-DC-Converter (2. Stage) and the battery [1]. Capacitive coupling to the device case and chassis occurs due to parasitic effects ( $C_{p,x}$ ) and filter capacitances ( $C_{CM}$ ,  $C_{Y,x}$ ). The diagram illustrates the common mode coupling paths and the resulting touch and leakage currents. It highlights the 'Result of  $i_{leak}$ ' (False Tripping of RCD) and 'Result of PE-Failure:  $i_t$ ' (Touch current). The circuit includes a Grid connection with RCD, a 2 Stage Filter, an AC-DC converter, a DC-DC converter (prim.), and a Battery. Parasitic capacitances are labeled as  $C_{p,AFE}$ ,  $C_{p,ZK+}$ ,  $C_{p,ZK-}$ ,  $C_{p,DC}$ ,  $C_{Y,EV+}$ , and  $C_{Y,EV-}$ . The diagram also shows the 'Sum and spread equally between DC-Rails' and the formula for calculating the total common mode capacitance:  $C_{CM} = C_0 + \frac{1}{2}(C_{p,DC} + \dots + C_{Y,EV+} + C_{Y,EV-})$ .

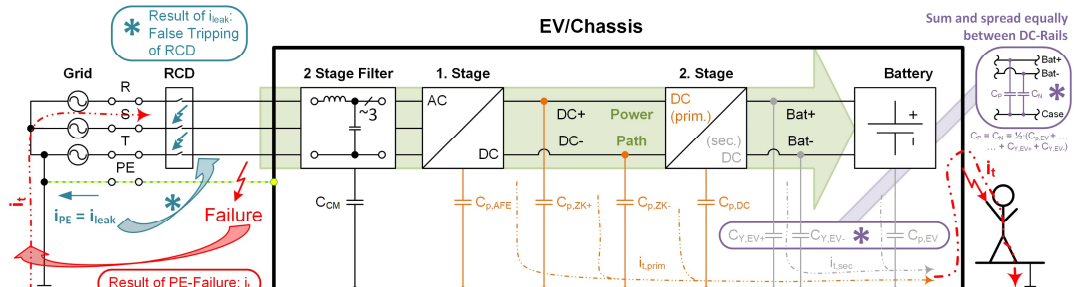


Figure 1: Example for a two-stage charging system

A major safety concern is the failure of the protective earth (PE) conductor. In this scenario, a person touching the chassis is coupled to all common mode voltage (CMV) sources within the power path referenced to ground, resulting in a certain touch current  $i_t$  flowing through the body. Isolated charging systems contain a transformer in the second stage, highly reducing the capacitive coupling due to the series connection of the transformer stray capacitance and the capacitive coupling of the charger secondary and EV (grey marking). Hence the major part of  $i_t$  equals  $i_{t,prim}$  (orange marking). The sum of all secondary coupling capacitors, equally spread between both DC-rails and PE is represented by  $C_P$  and  $C_N$  (purple marking). Non-isolated chargers allow to omit the transformer with the advantage of volume, weight and cost reduction and an improvement in efficiency. On the other hand,  $C_P$  and  $C_N$  are added to the touch current path, hence  $i_t$  equals the sum of  $i_{t,prim}$  and  $i_{t,sec}$ . Since the values of  $C_P$  and  $C_N$  may reach several  $\mu\text{F}$ , they will become the major coupling path and a significant increase of touch currents will occur [1]. Touch currents are limited to 3.5 mA at any operation scenario for Class 1 equipment by corresponding standards [10].

Beside the failure scenario of a broken PE conductor, the leakage current  $i_{leak}$  flowing through the PE conductor under normal operation is another important safety concern, since  $i_{leak}$  may lead to false tripping of the residual current device (RCD) at the supply side (grid side). As well as touch currents under fault conditions, leakage currents  $i_{leak}$  in the PE conductor at normal operation will increase in non-isolated charging systems since the coupling path is extended by  $C_P$  and  $C_N$ . The CMV driving these touch and leakage currents is influenced by the converter topology, DC link voltage, switching frequency, PWM, passive components and parasitic elements. This leads to a tremendous amount of combinations possible for system setup influencing  $i_t$  and  $i_{leak}$ . Hence, selecting and evaluating touch current behavior of certain combinations becomes a challenging process. With the aim to speed up that process and support integral system design, research is done to implement a workflow allowing flexibility in comparing different combinations and keeping time and simulation effort to a minimum.

## 1.2 Review on methods to analyze touch current behavior

Since touch and leakage currents are common mode (CM) currents, literature research is done regarding evaluation methods for CM behavior. In general, there are two main approaches within the results found: Either the system is transformed into CM equivalent circuits and results are analyzed within this reduced complexity (Group 1) or CM behavior is investigated by a full system simulation (Group 2). Figure 2 displays corresponding examples.

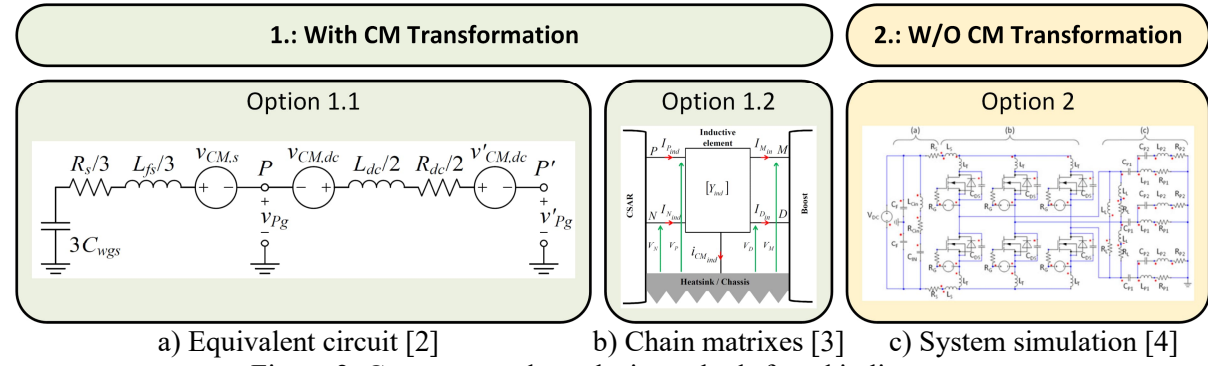


Figure 2: Common mode analysis methods found in literature

When transforming the system into CM domain (Group 1), two options are common in literature. Option 1.1 transforms the system one-by-one into a CM equivalent circuit. This approach is commonly used for CM analysis [2], [3] and [4], as well as for filter design [5], [6] and [7]. This method allows full flexibility in terms of circuit design, but complexity of its transfer function corresponds with the nesting of the circuit. With Option 1.2, the system is described with the help of chain matrices [3]. Each matrix describes a certain subsystem, for example a CM choke or a capacitive DM filter, with the usage of the quadrupole theory. The approach has its strength in daisy chaining several chain matrices. Furthermore, this method allows to cover mode conversion effects. On the other hand, it requires a high initial mathematical effort. Option 2 (Group 2) uses a full system time

domain simulation. It has its time demand in setting up the simulation model rather than in handling circuit equations. Option 2 allows full flexibility in terms of circuit design but has a high time demand in creating a model containing PWM, current regulation and grid synchronization. The precision of the result corresponds with the quality of the models used and the time step setting of the simulator. Hence, a single simulation run has a large time duration, especially when precise results are expected.

### 1.3 Selection of a touch current analysis method and creating the approach

Formulating the condition that time reduction and flexibility for CM analysis of certain system combinations are a priority, Option 1.1 becomes the method of choice. A workflow is implemented, calculating the CM behavior in time and frequency domain. The major steps of this workflow are summarized by Figure 3.

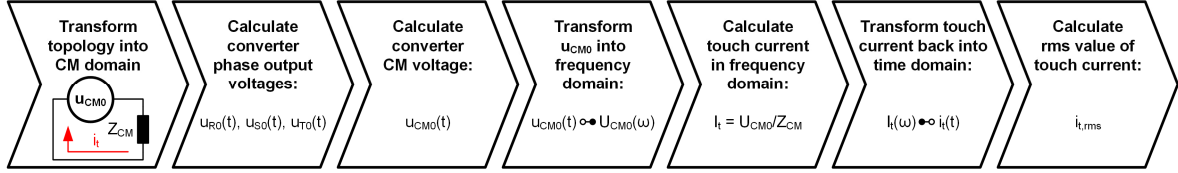


Figure 3: Workflow of the method for fast touch current prediction

Depending on the system specification, the second stage of a non-isolated charging system can be neglected. With respect to this fact, the implementation and validation of the workflow shown in Figure 3 is done for a single stage charging system working in normal operation and under the fault condition of a broken PE conductor. Since the literature cited focuses on filter design and CM analysis for electromagnetic compatibility (often in the context of drive applications), the aim of this work is to apply this approach on electrical safety topics of non-isolated charging systems, e.g. touch and leakage currents in the range of kHz. Furthermore, the research range is extended by investigating the influence of non-ideal passive component models on the calculation results.

## 2 Experimental setup

Figure 4 displays a 3-level neutral point clamped (NPC) converter used for the experimental validation. The converter operates with the switching frequency  $f_{sw} = 48$  kHz, the PWM includes third harmonic injection. The rated DC-Link-Voltage is 700 V and the load resistor is set to a 11 kW operation point. The converter has a filter including two differential mode (DM) stages ( $C_1$  &  $L_1$  and  $C_2$  &  $L_2$ ), as well as a CM choke  $L_{CM}$  and an additional CM path between  $C_2$  and case/ground (G) via the CM capacitor  $C_{CM}$ . The switches are silicon carbide (SiC) half bridge modules. The Line Impedance Stabilization Network (LISN) is model “NNLK-8121” from Schwarzbeck. It is used to ensure a defined situation at the supply side.

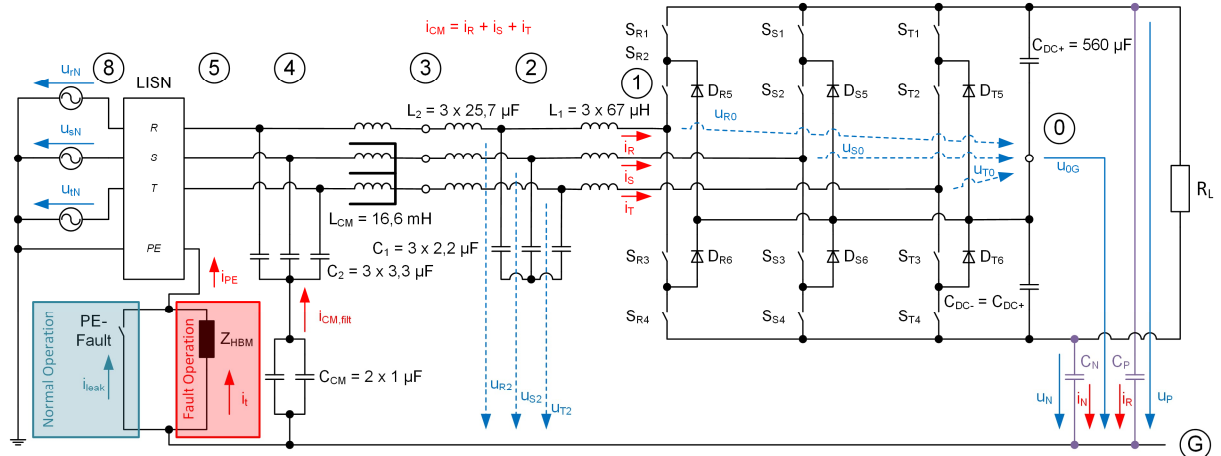


Figure 4: 3-Level NPC converter including its filter stages and a PE fault stimulation

### 3 Details on calculation method for common mode equivalent circuit and simulation

For the development of a single-phase CM equivalent circuit, definitions based on [2] are used:

$$u_{CM0} = \frac{u_{R0} + u_{S0} + u_{T0}}{3} \quad (1)$$

$$i_{CM} = i_R + i_S + i_T. \quad (2)$$

The following steps are executed to obtain the CM equivalent circuit of the experimental setup:

- Divide the entire topology into small sections.
- Define current and voltage expressions for each phase of the section.
- Transform equations for each section into CM domain.
- Daisy chain all sections to a complete CM equivalent circuit.

Figure 5 displays the entire CM equivalent circuit of Figure 4. The numbering of sections corresponds between both figures. A calculation example (green marking) is done for section 2-1-0-G-2 as follows.

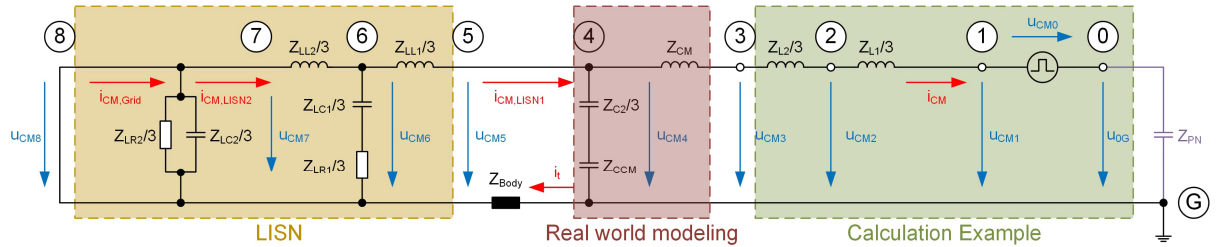


Figure 5: CM equivalent circuit of 3-level NPC converter

For each phase R, S and T of the setup shown in Figure 4, a voltage loop of this section is formulated:

$$Z_{L1} \cdot i_R + u_{R0} + u_{0G} - u_{R2} = 0 \quad (3)$$

$$Z_{L1} \cdot i_S + u_{S0} + u_{0G} - u_{S2} = 0 \quad (4)$$

$$Z_{L1} \cdot i_T + u_{T0} + u_{0G} - u_{T2} = 0. \quad (5)$$

The summation of the three loops (3) to (5) equals to:

$$Z_{L1} \cdot (i_R + i_S + i_T) + (u_{R0} + u_{S0} + u_{T0}) + 3u_{0G} - (u_{R2} + u_{S2} + u_{T2}) = 0. \quad (6)$$

Dividing (6) by 3 allows usage of the common mode definitions given in (1) and (2):

$$\frac{Z_{L1}}{3} \cdot i_{CM} + u_{CM0} + u_{0G} = u_{CM2}. \quad (7)$$

Equation (7) shows, that the impedance  $Z_{L1}$  of the first DM choke  $L_1$  has a contribution of one third of a single element value within the CM domain. The CMV driven by the converter is  $u_{CM0}$ . The connection point for the transformation of the next section on the ac-side is the CMV  $u_{CM2}$  at Point 2 referenced to ground. The transformation of the DC side can be daisy chained via the DC midpoint voltage  $u_{0G}$  referenced to ground. The entire CM equivalent circuit is achieved by transforming and daisy chaining the sections step-by-step. Their connection points are formulated as follows:

$$\frac{Z_{L2}}{3} \cdot i_{CM} + u_{CM2} = j\omega \frac{L_2}{3} \cdot i_{CM} + u_{CM2} = u_{CM3} \quad (8)$$

$$Z_{CM} \cdot i_{CM} + u_{CM3} = j\omega L_{CM} \cdot i_{CM} + u_{CM3} = u_{CM4} \quad (9)$$

$$\left( Z_{CCM} + \frac{Z_{C2}}{3} \right) \cdot (i_{CM,LISN1} - i_{CM}) = \left( \frac{1}{j\omega C_{CM}} + \frac{1}{j\omega 3C_2} \right) \cdot (i_{CM,LISN1} - i_{CM}) = u_{CM4} \quad (10)$$

$$Z_{Body} \cdot i_t + u_{CM4} = u_{CM5} \quad (11)$$

$$\frac{Z_{LL1}}{3} \cdot i_{CM,LISN1} + u_{CM5} = j\omega \frac{L_{L1}}{3} \cdot i_{CM,LISN1} + u_{CM5} = u_{CM6} \quad (12)$$

$$\begin{aligned} & \left( \frac{Z_{LC1}}{3} + \frac{Z_{LR1}}{3} \right) \cdot (i_{CM,LISN2} - i_{CM,LISN1}) = \dots \\ & \dots = \left( \frac{1}{j\omega 3C_{L1}} + \frac{R_{L1}}{3} \right) \cdot (i_{CM,LISN2} - i_{CM,LISN1}) = u_{CM6} \end{aligned} \quad (13)$$

$$\frac{Z_{LL2}}{3} \cdot i_{CM,LISN2} + u_{CM6} = j\omega \frac{L_{L2}}{3} \cdot i_{CM,LISN2} + u_{CM6} = u_{CM7} \quad (14)$$

$$\frac{u_{rN} + u_{sN} + u_{tN}}{3} = u_{CM8} = 0 \quad (15)$$

$$i_{CM,Grid} = i_{CM,LISN2} \quad (16)$$

$$Z_{PN} = \frac{1}{j\omega(C_P + C_N)}. \quad (17)$$

According to (15), the grid is assumed to be ideal. Hence, the filter elements  $C_{L2}$  and  $R_{L2}$  of the LISN are shorted. Furthermore,  $L_{CM}$  is assumed to have ideal coupling. The resulting CM current  $i_{CM}$  at normal operation is achieved by applying Ohm's Law on the CMV  $u_{CM0}$  produced by the converter and the resulting CM impedance  $Z_{CM,res}$ . The touch current  $i_t$  is calculated using the current divider calculation rule, since  $i_t$  is the fraction of  $i_{CM}$  not flowing through the filter structure  $C_{CM}$  and  $C_2$ :

$$i_{cm} = -\frac{u_{CM0}}{Z_{CM,res}} \quad (18)$$

$$i_t = \frac{\frac{Z_{C2}}{3} + Z_{CCM}}{\frac{Z_{C2}}{3} + Z_{CCM} + Z_{Body} + \left( \frac{Z_{LL2}}{3} \parallel \left( \frac{Z_{LC1}}{3} + \frac{Z_{LR1}}{3} \right) \right) + \frac{Z_{LL1}}{3}} \cdot i_{cm} = -Z_{CM,t} \cdot \frac{u_{CM0}}{Z_{CM,res}}. \quad (19)$$

The calculation software "Maple" is used for factorizing the resulting impedance equations for  $Z_{CM,res}$  and  $Z_{CM,t}$ . Matlab is used to compute all other calculation steps represented in Figure 3 and achieve results in frequency and time domain. The CMV pattern is created by sine-triangle comparison of three reference signals including third harmonic injection. The third harmonic amplitude is derived from the fundamental by multiplication with the factor 0.16667.

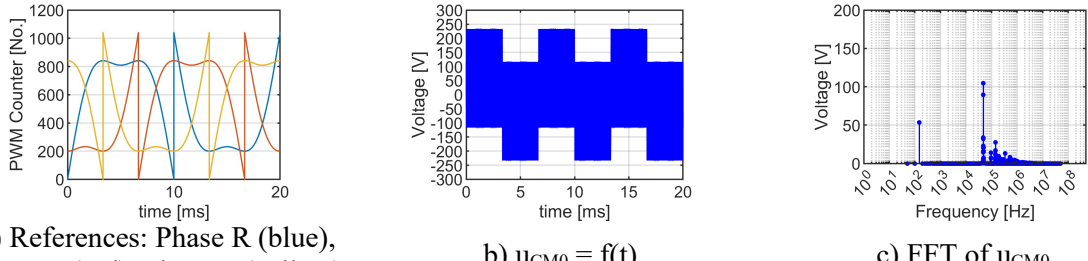


Figure 6: Creation of the converter common mode voltage  $u_{CM0}$

The PWM FPGA code of the experimental setup is implemented one by one within the Matlab calculation workflow: The sampling frequency of the reference and triangle signals is 100 MHz. The base of the triangle signal is a 11 Bit counter. Counter and reference values are positive integers, hence negative values are flipped. Figure 6 shows the three-phase reference values (a), the resulting CMV (b) achieved by applying (1) on the phase output voltages ( $u_{R0}$ ,  $u_{S0}$ ,  $u_{T0}$ ) of the converter and the FFT of the CMV (c) with its major components at the third harmonic,  $f_{SW}$  and its multiples.

## 4 Boundary condition: Human body model

For failure scenarios (break of PE conductor) resulting in a touch current  $i_t$  flowing through a person while touching the chassis, a human body model (HBM) is defined by corresponding standards [11], [12]. The equivalent circuit and its parameters can be found in Figure 7 a) and b).  $R_S$  and  $C_S$  are representing the skin, while  $R_B$  models the body itself. Since the human body is less sensitive for high frequency currents regarding startle response and the ability to let go, a first order filter utilized by  $R_1$  and  $C_1$  is added in parallel to  $R_B$ . For charging applications, evaluation of  $i_t$  is done on the basis of the peak value of the rated touch current  $i_{t,rated}$ , rather than on the raw touch current  $i_{t,raw}$ . The value of  $i_{t,rated}$  is measured via the voltage  $u_2$  of  $C_1$  divided by  $500 \Omega$  [12].

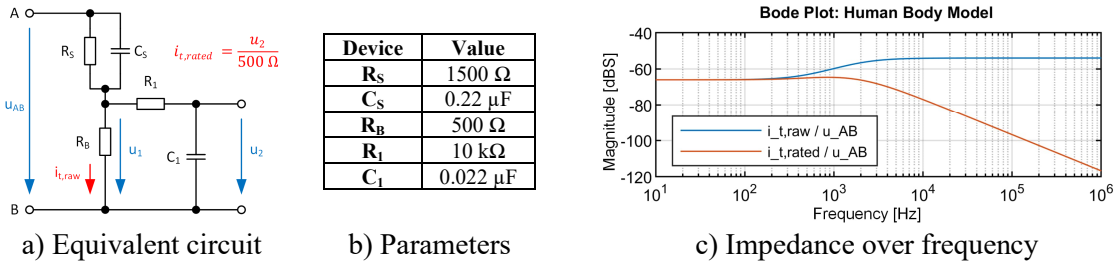


Figure 7: Human body model [10] and [12]

In the bode plot of  $i_{t,rated}$  shown in Figure 7 c), it can be clearly seen that the corner frequency is located between 2 kHz and 3 kHz. The bode plot finishes at 1 MHz, since the human body model is defined up to 1 MHz. This is the upper frequency limit for electrical safety defined in [12]. For further investigations of non-ideal modeling, two intermediate conclusions can be drawn:

- Frequency-dependent effects are relevant only in the frequency range from DC up to 1 MHz. Since [12] rates 1 MHz as corner frequency between electrical safety and electromagnetic compatibility, 1 MHz is used as upper frequency limit for investigations on fault operation ( $i_t$ ) and normal operation ( $i_{leak}$ ).
- Effects from 2 kHz onwards have a decreasing impact on  $i_{t,rated}$  with a slope of -20dB/dec.

## 5 Passive components: Impedance curves, non-ideal models and expectations on their influence

The impedance curves over frequency of all passive components are measured with the impedance analyzer Bode 100. A summary of the measurement results is given in Figure 8.

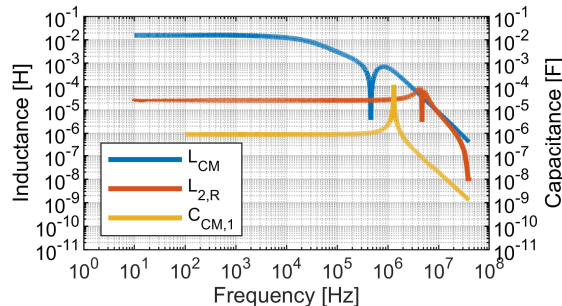


Figure 8: Passive component impedance curves

Table 1: Non-ideal models and their parameters

Element	$L_{DM1}$	$L_{DM2}$	$C_{DM2}$	$C_{CM}$
$L / C$	$67 \mu\text{H}$	$26 \mu\text{H}$	$2.9 \mu\text{F}$	$0.9 \mu\text{F}$
$C_{par} / L_{ESL}$	$16 \text{ pF}$	$45 \text{ pF}$	$16 \text{ nH}$	$17 \text{ nH}$
$R_{ESR} [\text{m}\Omega]$	$\leq 0.1 \Omega$	$\leq 0.1 \Omega$	$145 \text{ m}\Omega$	$159 \text{ m}\Omega$
$f_{res}$	$4.8 \text{ MHz}$	$4.6 \text{ MHz}$	$0.8 \text{ MHz}$	$1.3 \text{ MHz}$
Equivalent Circuit				

Due to the limitation of space, only one impedance curve per element type ( $L_{CM}$ ,  $C_{CM}$ ,  $L_2$ ) is presented. In general, the DM-inductors and all capacitors show very similar curves: Their impedance is very stable up to the resonance point and only small variations in resonance frequencies and nominal values occur. Corresponding values can be found in Table 1.

Equivalent circuit models covering the behavior of all DM inductances and all capacitors are taken from [8] and displayed at the last row of Table 1. The resonant points of both DM inductances are located at the area between 4 and 5 MHz, which is outside of the definition of the HBM, ending up at 1 MHz. Due to that reason, the influence of a non-ideal DM inductance model on the touch and leakage current is considered as neglectable.

The resonance points of the capacitors are located at the area of 1 MHz, which is the upper definition limit of the scope of this work. Hence the effect of non-ideal capacitor models on the calculation results is considered to be small. The DM capacitors  $C_1$  are omitted since they have no contribution to the CM domain.

The impedance of the CM choke is unstable and changes over frequency, even in the range of kHz. Since the impedance of  $L_{CM}$  changes at the frequency range of  $f_{SW}$  and their multiples, a noticeable impact on the touch and leakage current prediction is expected and the focus in the results section is set on this device. For ease of implementation, the  $L_{CM}$  characteristic is implemented as a look-up table (LUT).

## 6 Results

The following sections compare prediction results using ideal and non-ideal models and laboratory measurement results. Since  $L_{CM}$  is expected to have the highest impact on the prediction result, the non-ideal prediction results are split into two groups using only a non-ideal model of  $L_{CM}$  and using non-ideal models of  $L_{CM}$ ,  $C_{CM}$  and  $C_2$ . Due to the boundary conditions of Section 4, the frequency domain plots are cut off at 1 MHz. The converter operates with a DC-Link Voltage of  $V_{DC} = 700$  V and  $P_{charge} = 11$  kW. Due to the limitation of space, only one set point with  $C_P = C_N = 1 \mu F$  is presented. Results investigating the variation of  $C_P$  and  $C_N$  are given in Table 2.

### 6.1 Fault operation: Effects of non-ideal $L_{CM}$ , $C_{CM}$ and $C_2$ on $i_{PE} = i_t$ and $i_{CM}$

Figure 9 shows a comparison for the rated touch current  $i_{t,rated}$  through the HBM. All calculation results only have one major component at 150 Hz due to the third harmonic injection of the PWM.

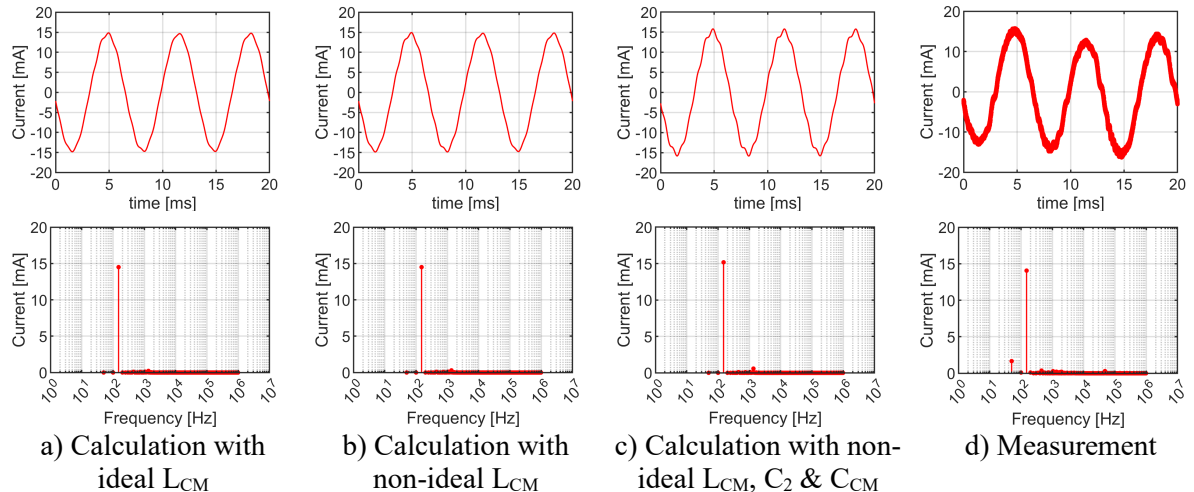


Figure 9: Prediction and measurement of  $i_{t,rated}$  through HBM, converter working under PE-Fault

The measurement matches almost perfectly with the calculations: There is one major component with an amplitude of approximately 15 mA at 150 Hz. But there is no sensitivity of  $i_{t,rated}$  regarding the

modeling of  $L_{CM}$  within the calculation. The usage of non-ideal capacitor models cause a small increase of  $i_{t,rated}$ . The non-ideal impedance of  $C_2$  and  $C_{CM}$  slightly increases, since their actual values are smaller than their ideal nominal value, leading to a small shift of current from the path via  $C_2$  and  $C_{CM}$  to the parallel path via the HBM. An additional unexpected component at 50 Hz occurs within the measurement. Since the unused neutral conductor port at the LISN shows an AC offset with several volts amplitude and 50 Hz frequency against PE, an asymmetry on the grid side is assumed to cause the additional 50Hz content in this and all other measurements.

The waveforms of the time domain plots of all other results only show small changes: The 150 Hz sine wave remains as a basis, only the amplitude and the width of the noise band varies in dependency of the operation point. Since space is limited only FFT plots are shown.

Figure 10 compares the CM current  $i_{CM}$  at the converter input between the prediction method with ideal and non-ideal models and the laboratory measurement result. Two basic trends apply for all results: All amplitudes increase significantly compared to Figure 9 and additional components at  $f_{sw} = 48$  kHz and their multiples occur.

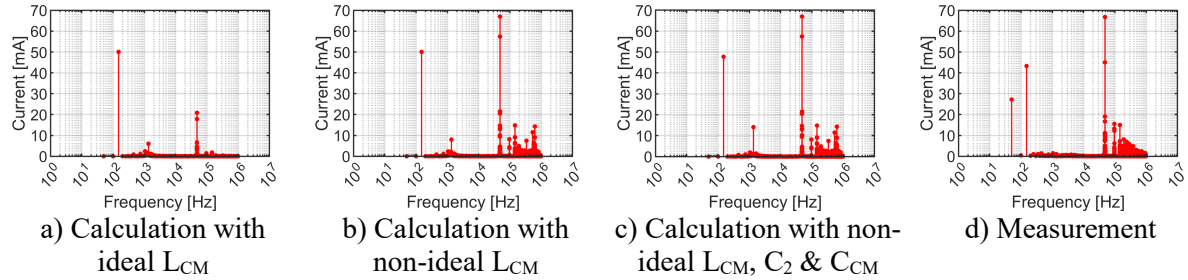


Figure 10: Prediction and measurement of  $i_{CM}$ , converter working under PE-Fault

When comparing the calculation results, it can be clearly seen that there is an increase of the  $f_{sw}$  component by a factor of 3 when using the non-ideal model of  $L_{CM}$ , whereas the 150 Hz component shows no significant change. This corresponds with the decreasing inductance of  $L_{CM}$ , starting with approximately 15 mH and decreasing to 5 mH at  $f_{sw}$ . The impedance curve of  $L_{CM}$  can be found in Figure 8. The 150 Hz component shows no change regarding to the  $L_{CM}$  model, since  $L_{CM}$  has a constant inductance at that frequency range. On the other hand, the 150 Hz component decreases slightly when using non-ideal capacitors models due to the slight increase of the resulting CM impedance. Adding the measurement results to the comparison it can be clearly seen that there is a good match between measurement and prediction when using non-ideal models regarding the major components of  $i_{CM}$  at 150 Hz and  $f_{sw}$ , whereas the prediction with the ideal modeling is inaccurate at  $f_{sw}$ . The major improvement within the calculation results is due the non-ideal  $L_{CM}$  model. On the other side, the non-ideal capacitors models have a small influence on the calculation result.

A comparison of  $i_{CM}$  to the previous results of  $i_{t,rated}$  in Figure 9 shows that there is a reduction of the third harmonic of  $i_{t,rated}$  by more than a factor of 3. Furthermore,  $i_{t,rated}$  didn't show any components at  $f_{sw}$  and its multiples. In other words, during failure scenarios, the parallel internal CM path through  $C_{CM}$  and  $C_{DM2}$  is a very efficient current divider, keeping all high frequency content and a fraction of the third harmonic within the internal common mode loop rather than allowing that current to flow as  $i_t$  through the PE conductor and the HBM. Since the touch current is reduced to a problem of the third harmonic in this setup, further improvement could be achieved by minimizing or eliminating the third harmonic injection to pass the standard limit for the rated touch current of 3.5 mA.

## 6.2 Normal operation: Effects of $L_{CM}$ , $C_{CM}$ and $C_2$ on $i_{CM}$ and $i_{PE} = i_{leak}$

The analysis is repeated during normal operation, hence the PE fault switch is closed (see Figure 4). Figure 11 displays the FFT plots of  $i_{CM}$ , achieved from calculation with ideal and non-ideal passive models and from laboratory measurement. When looking at the calculation results of Figure 11 a) to c), two major trends compared to fault operation in Figure 10 occur: First of all, the amplitude of the

150 Hz component increases significantly by a factor of 2, which can be explained by a decrease in the CM path impedance of the PE conductor due to the elimination of the HBM. Secondly, the influence of the non-ideal  $L_{CM}$  model appears the same as at failure mode: The  $f_{SW}$  component increases significantly within the calculation results, whereas the 150 Hz component remains the same.

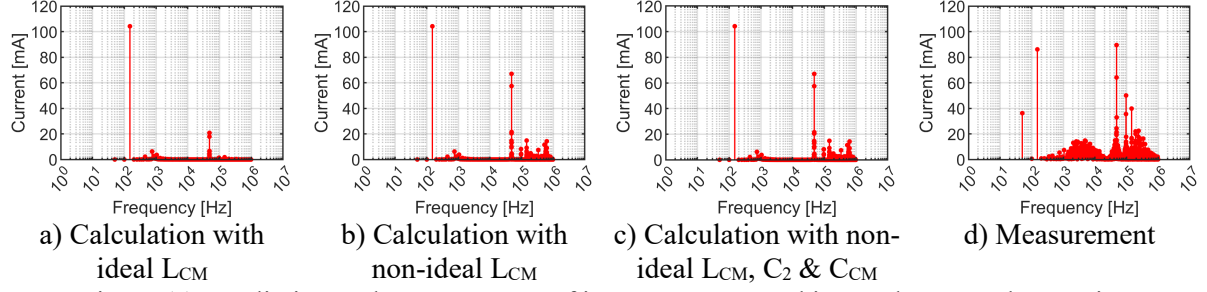


Figure 11: Prediction and measurement of  $i_{CM}$ , converter working under normal operation

The non-ideal capacitor models have no visible effect on the calculation result. The calculation with the non-ideal models and the measurement show major components at 150 Hz and  $f_{SW}$  as well, but the amplitudes do not match perfectly.

The comparison of the PE conductor current  $i_{PE}$ , which is  $i_{PE} = i_{leak}$  under normal operation condition, is displayed in Figure 12. The influence of the non-ideal  $L_{CM}$  model appears the same way as with  $i_{CM}$  in Figure 11: The  $f_{SW}$  component increases whereas the 150 Hz component remains at the same amplitude and the impact of the non-ideal capacitor models is minimal.

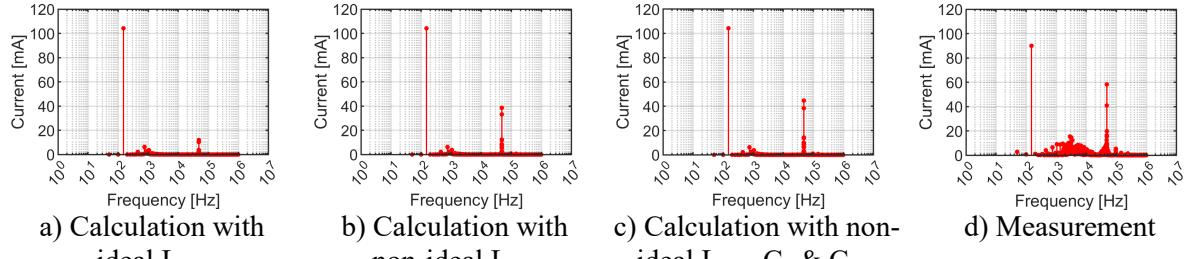


Figure 12: Prediction and measurement of  $i_{PE}$ , converter working under normal operation

When comparing the frequency domains of  $i_{PE}$  in Figure 12 under normal operation and  $i_{t,rated}$  under fault operation in Figure 9, several trends can be seen. First, the 150 Hz component increases by factor of 6 from 15 mA to approximately 105 mA. This can also be explained by the decrease of impedance of the ground loop due the elimination of the HBM. Secondly it can be clearly seen that the influence of the parallel CM path through  $C_{CM}$  and  $C_{DM2}$  decreases significantly under normal operation. Besides the 150 Hz component,  $i_{PE}$  has an additional major component at  $f_{SW}$ , whereas  $i_{t,rated}$  is defined by the 150 Hz component itself. For normal operation, the CM path through the filter is less efficient and bypasses only parts of the high frequency CM currents from the ground loop.

For consumer households, it is assumed that the typical RCDs have a trip point of  $i_{PE} \geq 30$  mA [9]. These RCDs provide protection against indirect touch and additional protection against direct touch [13]. Under this assumption, false tripping at normal operation is expected, since  $i_{PE}$  is above that limit by factor of 3 at 150 Hz. RCDs of type B and B+ have a decreasing sensitivity at higher frequencies. Their trip points at  $f_{SW}$  are at 8000 mA (Type B) and 330 mA (Typ B+) according to [13]. Therefore, false tripping due to the  $f_{SW}$  component is not expected.

Finally, Table 2 shows a comparison of RMS values between calculation and measurement results, when the coupling capacitor is increased. The calculations results are given for non-ideal models of  $L_{CM}$ ,  $C_2$  and  $C_{CM}$ . It can be seen that the dependency between the current in the PE conductor and the increasing capacitive coupling is significantly higher during normal operation ( $i_{leak}$ ) than during a fault

condition ( $i_{t,\text{rated}}$ ). Furthermore, the difference between calculation and measurement is higher during normal operation. Both effects can be explained with the absence of the HBM and therefore the reduction of impedance of the ground loop during normal operation. Further research on the setup of the CM structure will be done with the aim of finding a CM structure allowing  $i_{t,\text{rated}}$  being independent from  $C_P$  and  $C_N$ .

All calculation points have a difference between calculation and measurement in the range of single-digit values of mA, which underlines the precision of the chosen calculation approach.

Table 2: Comparison of RMS values between calculation using non-ideal models of  $L_{\text{CM}}$ ,  $C_2$ , and  $C_{\text{CM}}$  and measurement

a) Comparison of $I_{t,\text{rated},\text{rms}}$ during PE fault				b) Comparison of $I_{\text{PE},\text{rms}} = I_{\text{leak},\text{rms}}$ during normal operation			
$C_P, C_N [\text{nF}]$	$I_{\text{calc}} [\text{mA}]$	$I_{\text{meas}} [\text{mA}]$	$\Delta I [\text{mA}]$	$C_P, C_N [\text{nF}]$	$I_{\text{calc}} [\text{mA}]$	$I_{\text{meas}} [\text{mA}]$	$\Delta I [\text{mA}]$
<b>440</b>	6.7	6.0	0.7	<b>440</b>	59.3	55.9	3.4
<b>1000</b>	10.7	9.3	1.4	<b>1000</b>	87.7	97.5	-9.8
<b>3300</b>	15.8	13.5	2.3	<b>3300</b>	267.8	259.0	8.8

## 7 Conclusion

This paper presents a fast and precise CM analysis method applied to electrical safety considerations of non-isolated EV chargers. The discrepancy of RMS values between measurement and calculation is in the range of single-digit mA. The runtime of the calculation for a certain setpoint is within a timeframe of 60-90 s. Both parameters underline the precision and speed of the chosen calculation approach.

For electrical safety considerations, a frequency limit of 1 MHz is defined in corresponding standards. This limit helps to reduce the number of passive elements considered for non-ideal component modeling. In this setup, the CM inductor was identified as an important element for non-ideal modeling due to its variable inductance over frequency in the range of kHz. The influence of non-ideal capacitor models was minimal.

For this given setup, the converter CM current  $i_{\text{CM}}$  turned out to be highly sensitive to the non-ideal model of  $L_{\text{CM}}$ , which is very important for filter design. On the other hand, the touch current  $i_{t,\text{rated}}$  itself showed no sensitivity to detailed  $L_{\text{CM}}$  modeling. Further investigations will be done in an upcoming publication, considering whether the non-sensitivity of  $i_{t,\text{rated}}$  for non-ideal passive component models can be generalized.

For failure scenarios, a parallel CM path ( $C_2, C_{\text{CM}}$ ) within the filter system offers as a very powerful method to eliminate high frequency currents from the touch current path and to reduce  $i_t$  to a low frequency problem. The corresponding standard peak value limit for  $i_{t,\text{rated}}$  is 3.5 mA. For this setup, a revision of the PWM (reducing or eliminating the third harmonic injection) is a practical approach to achieve the required standard.

Finally, this work clearly points out that the leakage current in the PE conductor under normal operation condition is another challenging situation of non-isolated charging systems. The 150 Hz component increases by factor six at normal operation compared to the touch current at fault condition. Furthermore, high frequency content is added to the spectrum of  $i_{\text{leak}}$ . False tripping of the RCD due to the tremendous 150 Hz component is expected.

## References

- [1] Y. Zhang et al.: Leakage Current Issue of Non-Isolated Integrated Chargers for Electric Vehicles, 2018 IEEE Energy Conversion Congress and Exposition (ECCE), Portland, OR, 2018, pp. 1221-1227, doi: 10.1109/ECCE.2018.8558133.
- [2] A. D. Brovont, S. D. Pekarek: Equivalent Circuits for Common-Mode Analysis of Naval Power Systems, 2015 IEEE Electric Ship Technologies Symposium (ESTS), pp. 245-250, Jul. 2015, doi: 10.1109/ESTS.2015.7157897.
- [3] C. Saber, D. Labrousse, B. Revol, A. Gascher: A Combined CM & DM Conducted EMI Modeling approach, Proc. of the 2017 International Symposium on Electromagnetic Compatibility - EMC EUROPE 2017, Sep. 2017, doi: 10.1109/EMCEurope.2017.8094616.
- [4] D. Labrousse, B. Revol, C. Gautier, F. Costa: Fast Reconstitution Method (FRM) to Compute the Broadband Spectrum of Common Mode Conducted Disturbances, IEEE Transactions on Electromagnetic Compatibility, vol. 55, no. 2, pp. 248-256, Apr. 2013, doi: 10.1109/TEMC.2012.2219056.
- [5] G. Mondal, J. Robinson and M. Finkenzeller: Modeling and Design of Common Mode and Differential Mode Filter for PWM Converters, 10th International Conference on Power Electronics and ECCE Asia (ICPE 2019-ECCE Asia), 2019, pp. 2191-2198, doi: 10.23919/ICPE2019-ECCEAsia42246.2019.8796878.
- [6] D. O. Boillat, J. W. Kolar, J. Mühlenthaler: Volume Minimization of the Main DM/CM EMI Filter Stage of a Bidirectional Three-Phase Three-Level PWM Rectifier System, 2013 IEEE Energy Conversion Congress and Exposition, Oct. 2013, pp. 2008-2019, doi: 10.1109/ECCE.2013.6646954.
- [7] M. H. Hedayati, A. B. Acharya, V. John: Common-Mode Filter Design for PWM Rectifier-Based Motor Drives, IEEE Transactions on Power Electronics, vol. 28, no. 11, pp. 5364-5371, Nov. 2013, doi: 10.1109/TPEL.2013.2238254.
- [8] G. Zschau: EMV-gerechte Schaltungsauslegung (LE), Vorlesungsskript, TU Dresden, 2009.
- [9] Hofheinz et al.: Elektrische Sicherheit in der Elektromobilität, VDE-Schriftenreihe Normen verständlich 174, 2019, ISBN 978-3-8007-4882-2.
- [10] IEC: IEC 61851-1, Electric vehicle conductive charging system – Part 1: General requirements, International Standard, Feb. 2017, ISBN 978-2-8322-3766-3.
- [11] IEC: IEC 61851-23, Electric vehicle conductive charging system – Part 23: DC electric vehicle charging station, International Standard, Mar. 2014, ISBN 978-2-8322-1440-4.
- [12] IEC: Methods of measurement of touch current and protective conductor current (IEC 60990:2016), German version EN 60990:2016, National Standard, Mar. 2017, ICS 13.260
- [13] Siemens AG: Fehlerstromschutzeinrichtungen, Technik-Fibel, Feb. 2018, Purchase Order Number EMLP-T10158-00-00DE